J Adv Ceram

Research Article

Entropy enhancing toughness of diborides: First-principles insights and experimental validation

Yang Lin[1,2], Wengang Bu[3], Pengfei He[3], Jingjin He[1,2], Xiubing Liang[3], Zulai Li[1,2], Yehua Jiang[1,2], Xingjun Liu[4], Jing Feng[1], Xiaoyu Chong[1,2,✉]

Cite this article: Lin Y, Bu W, He P, et al. *J Adv Ceram* 2026, **15**(4): 9221266. https://doi.org/10.26599/JAC.2026.9221266

ABSTRACT: The intrinsically low toughness and high brittleness of diboride ceramics are major limitations restricting their widespread application. Toughness can be enhanced through increased configurational entropy; however, the physical mechanisms underpinning this entropy-induced toughening remain poorly understood. In this study, a comprehensive approach from element screening to mechanistic elucidation and experimental validation is undertaken to address these gaps. First, a theory-guided element screening strategy is employed. Starting from dilute solid-solution models and integrating calculation of phase diagrams (CALPHAD) composition–property fitting, Ta, Nb, Mo, Hf, and V are identified for their synergistic optimization of hardness and toughness. Subsequently, the evolution of toughness with increasing configurational entropy is assessed using bulk modulus/shear modulus (B/G), fracture toughness (K_{IC}), and related metrics. The calculations are validated against available experimental data, revealing an almost monotonic trend, with the six-component system exhibiting a K_{IC} exceeding 5.8 MPa·m$^{1/2}$—approximately double that of the single-component counterpart. A systematic analysis of the lattice distortion and crystal orbital Hamilton population is performed for diborides containing two to six alloying elements. From a bond-strength perspective, the toughening mechanism originates from increased thermodynamic disorder, which broadens and flattens the bond-strength distribution, giving rise to a "bond-strength trap". Experimental validation is conducted on the (TiTa)B_2 and (TiNb)B_2 systems with pronounced bond-strength contrast, as well as the ternary (TiTaNb)B_2 system. The results corroborate the predicted electronic bonding evolution, while further analysis of phonon force constants and stacking fault energies indicates that the synergy between strengthened M–B bonds and reduced dislocation slip barriers underpins the enhanced toughness.

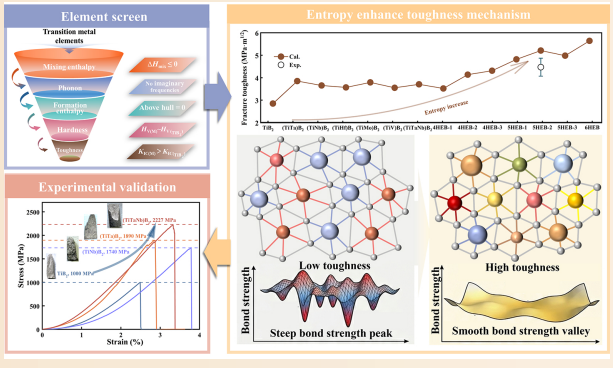

KEYWORDS: thermodynamics; first-principles calculations; calculation of phase diagrams (CALPHAD); high-entropy diborides; fracture toughness

1 Introduction

The collaborative optimization of strength and toughness remains a persistent challenge in materials science, particularly for ceramic materials. Diboride, for instance, possesses an impressive hardness exceeding 30 GPa, yet its fracture toughness remains low, typically in the range of 2–3 MPa·m$^{1/2}$. This severe trade-off significantly restricts its widespread application in critical fields such as aerospace engineering [1–3], cutting tools, and wear-resistant components [4–6]. In application scenarios such as cutting tools and high-temperature protective coatings, crack initiation and propagation in borides constitute the primary failure mechanisms. Enhancing fracture toughness is therefore critical for suppressing catastrophic fracture of structural components and mitigating coating delamination during service, thereby improving the reliability of boride-based materials and reducing their overall application cost. To overcome this limitation, high-entropy design strategies have recently attracted considerable attention. By incorporating multiple principal elements to increase the system's configurational entropy, this approach promotes a disordered atomic environment that enables the tailoring of bonding characteristics and deformation mechanisms—ultimately offering a promising route to synergistically optimize mechanical properties [7,8].

[1] Faculty of Material Science and Engineering, Kunming University of Science and Technology, Kunming 650093, China. [2] National-Local Joint Engineering Research Center for Technology of Advanced Metallic Solidification Forming and Equipment, Kunming 650093, China. [3] National Defense Science and Technology Innovation Research Institute, PLA Academy of Military Sciences, Beijing 100071, China. [4] School of Metallurgical and Energy Engineering, Kunming University of Science and Technology, Kunming 650093, China.

✉ Corresponding author. E-mail: xiaoyuchong@kust.edu.cn

Received: November 19, 2025; Revised: February 20, 2026; Accepted: February 20, 2026

Recent studies have shown that introducing high configurational entropy into ceramic systems by increasing the number of principal metallic components can generate strong lattice distortion and sluggish atomic diffusion effects, thereby improving both mechanical strength and fracture toughness [9–11]. This high-entropy design strategy, originally demonstrated in metallic systems, has now been extended to carbides, nitrides, and borides [9,10,12]. For instance, Li *et al.* [13] synthesized single-phase (HfNbTaTiW)C with fine grains via carbon thermal reduction at 1700 °C and spark plasma sintering (SPS) at 1800 °C, achieving a nanohardness of 28.16 GPa and fracture toughness of 4.84 MPa·m$^{1/2}$—outperforming both its constituent monocarbides and most existing multication transition metal carbides. Similarly, Tang *et al.* [14] and Liu *et al.* [15] demonstrated the exceptional oxidation resistance of high-entropy borides (HEBs) and proposed a hardening mechanism linked to lattice distortion. Qin *et al.* [16] successfully synthesized five-component HEBs by SPS, further reinforcing the promise of entropy-engineered design. Liu *et al.* [17] reported that high-entropy (TiZrHfNbTa)B_2 and its SiC-reinforced composite exhibit flexural strengths of 339±17 and 447±45 MPa, with fracture toughness reaching 4.85±0.33 MPa·m$^{1/2}$. At present, the underlying physical mechanisms governing entropy-driven toughening in diborides remain poorly understood. In particular, the correlation between configurational entropy and key microstructural parameters such as bond strength, lattice distortion, and electronic structure has not been systematically established. While empirical results confirm mechanical enhancement, the microscopic origin, especially how entropy alters atomic-scale interactions such as chemical bonding and stacking fault behavior, warrants deeper theoretical and experimental analysis.

To address this gap, first, based on TiB_2 as an initial system, a comprehensive high-throughput screening of 29 alloying elements is performed using density functional theory (DFT), assessing thermodynamic stability, mechanical properties, and phonon dispersion to identify elements capable of enhancing toughness, as outlined in Fig. 1. TiB_2, with its hexagonal AlB_2-type structure (space group *P6/mmm*) [18,19], consists of alternating layers of boron and titanium atoms, where strong B–B covalent bonds form planar honeycomb networks and Ti–B interactions further stabilize the lattice [20,21]. Starting from this single-component diboride enables clear tracking of how increasing configurational entropy affects bonding and deformation behavior. Second, we delve into the physical origin of entropy-enhanced toughness using both advanced first-principles simulations and experimental verification. Specifically, we investigate how configurational entropy influences lattice distortion, phonon force constants, stacking fault energies, and electronic interactions using crystal orbital Hamilton population (COHP) analysis. Multicomponent diborides synthesized via hot pressing are characterized through nanoindentation and compressive testing to validate the predicted trends. The results confirm that configurational entropy induces a wider and shallower bond strength distribution, reduces the directionality of M–B bonds, and facilitates dislocation mobility by lowering the stacking fault energy.

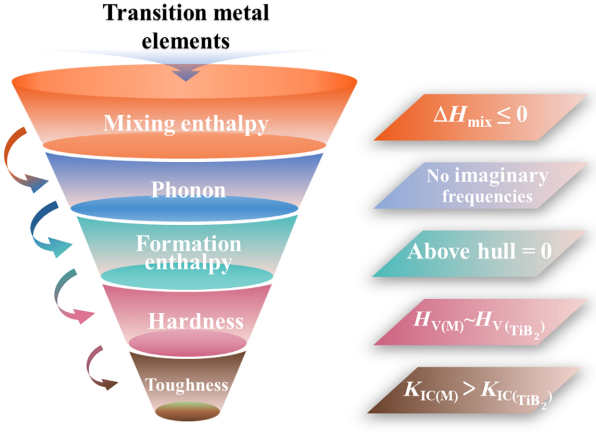

Fig. 1 Screen strategy of alloying elements for stability and mechanical properties.

2 Computational method and details

2.1 DFT calculation

The $Ti_{17}MB_{36}$ dilute solid solution structures are constructed as a 2 × 3 × 3 supercell including 54 atoms under periodic boundary conditions. Multicomponent diborides containing 2 to 6 kinds of elements are modeled using the special quasirandom structure (SQS) approach implemented in the alloy theoretic automated toolkit (ATAT) [22], and the supercell is given in Fig. S1 in the Electronic Supplementary Material (ESM). All first-principles calculations are performed on the basis of DFT as implemented in the Vienna *ab initio* simulation package (VASP) [23–25]. Scalar relativistic projector augmented wave (PAW) [26] pseudopotentials and the generalized gradient approximation (GGA) of Perdew–Burke–Ernzerhof for solids (PBEsol) [27,28] are used in the calculation. To ensure convergence of calculation accuracy, the maximum cutoff energy of the plane wave is set as 450 eV, and the Monkhorst–Pack scheme [29,30] is used to select *k*-points in the first Brillouin region. The COHP analyses were carried out using the Local Orbital Basis Suite Toward Electronic-Structure Reconstruction (LOBSTER) program. The *k*-mesh is set at a 0.2 Å^{-1} spacing with an Γ-centered mesh. The cutoff energy and *k*-mesh were subjected to rigorous convergence tests, as shown in Fig. S2 in the ESM. The detailed chemical components of the high-entropy system are as follows: (TaVNbTi)B_2 (4HEB-1), (MoNbTaTi)B_2 (4HEB-2), (TaHfNbTi)B_2 (4HEB-3), (NbTaTiMoV)B_2 (5HEB-1), (MoTiTaNbHf)B_2 (5HEB-2), (VTiTaNbHf)B_2 (5HEB-3), and (TiTaNbHfMoV)B_2 (6HEB).

2.2 Mixing enthalpy

The thermodynamic stability of materials can be evaluated by mixing enthalpy, which is defined as the energy relative to two pure substances in the same structures, with Eq. (1) [31]:

$$\Delta H_{\text{mixing}} = \frac{E_{\text{total}} - 17E_1 - E_2}{18} \quad (1)$$

where ΔH_{mixing} represents the mixing enthalpy of the $Ti_{17}MB_{36}$ dilute solid solution, E_{total} is the total energy, and E_1 and E_2 represent the total energy of TiB_2 and MB_2 per atom. For some stable crystals of MB_2 without the HCP structure, the Birch–Murnaghan equation of state (EOS) is adopted to fit the energy-volume curve for searching the equilibrium volume [32]. The EOS is given as Eq. (2):

$$E(V) = E_0 + \frac{9V_0B_0}{16}\left[\left(\left(\frac{V_0}{V}\right)^{\frac{2}{3}} - 1\right)^3 B_0' + \left(\left(\frac{V_0}{V}\right)^{\frac{2}{3}} - 1\right)^2 \left(6 - 4\left(\frac{V_0}{V}\right)^{\frac{2}{3}}\right)\right] \quad (2)$$

where E_0, V_0, B_0, and B_0' are the static total energy, equilibrium volume, bulk modulus, and the first derivatives of the bulk modulus to pressure, respectively. The static total energy is calculated by first-principles calculations for stable pure crystals.

According to Redlich–Kister polynomials and the regular solution model [33,34], the excess Gibbs energy term (G_m) of $Ti_{17}MB_{36}$ dilute solid solution is expressed as Eq. (3):

$$G_m = x_i x_j \sum_n {}^n L^{\varphi}_{i,j}(x_i - x_j)^n \tag{3}$$

where ${}^n L^{\varphi}_{i,j}$ is the n-order interaction parameter between elements i and j and represents the nonideal contribution of mixed Gibbs energy, which can be obtained by fitting the n-order polynomial of DFT calculation data.

2.3 Elastic properties

The elastic constants of the materials are calculated by using the stress–strain method defined by Hook's law as Eq. (4):

$$\sigma_{ij} = C_{ijkl}\varepsilon_{kl} \tag{4}$$

where C_{ijkl} is the elastic constant, and σ_{ij} and ε_{kl} are the tensors of stress and strain, respectively. The bulk modulus (B) and the shear modulus (G) calculated by the Voigt–Reuss–Hill (VRH) approximation method [35] are shown in Eqs. (5) and (6). To date, several semiempirical theoretical models have been developed to assess the hardness of materials [36]. Vickers hardness (H_v) is calculated by the Tian model in our study [37,38]. Poisson's ratio (v) and Young's modulus (E) [39] are calculated by B and G as shown in Eqs. (7) and (8):

$$B_{VRH} = \frac{1}{2}(B_V + B_R) \tag{5}$$

$$G_{VRH} = \frac{1}{2}(G_V + G_R) \tag{6}$$

$$E = 9\frac{B_{VRH}G_{VRH}}{3B_{VRH} + G_{VRH}} \tag{7}$$

$$v = \frac{3B_{VRH} - 2G_{VRH}}{2(3B_{VRH} + G_{VRH})} \tag{8}$$

$$H_V = 0.92\left(\frac{B}{G}\right)^{-1.137} G^{0.708} \tag{9}$$

where B_V, B_R, and B_{VRH} as well as G_V, G_R and G_{VRH} represent the bulk modulus and shear modulus obtained by the Voigt–Reuss–Hill approximation methods [40], respectively. Fracture toughness (K_{IC}) represents the ability of materials to prevent crack propagation, which can measure the safety of materials. However, the theoretical prediction of K_{IC} is harsh and difficult. According to Mazhnik and Oganov [41], K_{IC} can be estimated by Eq. (10):

$$K_{IC} = \alpha_0^{-1/2} V_0^{1/6} (\zeta(v)E)^{3/2} \tag{10}$$

where α_0 = 8840 GPa, and $\zeta(v)$ is a dimensionless function v and can be expressed as Eq. (11):

$$\zeta(v) = \frac{1 - 13.7v + 48.6v^2}{1 - 15.2v + 70.2v^2 - 81.5v^3} \tag{11}$$

Based on the elastic constants and elastic modulus of pure MB_2 and the dilute solid solution model $(TiM)B_2$ of the HCP structure, the 0-order interaction parameters of its elastic modulus and elastic constants can be obtained by Eqs. (12)–(14) based on CALPHAD modeling:

$$C_{lm} = {}^0 C_{lm} + \Delta C_{lm} \tag{12}$$

$${}^0 C_{lm} = \sum x_i^0 C_{lm}^i \tag{13}$$

$$\Delta C_{lm} = \sum_i \sum_{j>i} x_i x_j \sum_{n=0} {}^n I_{lm}^{ij}(x_i - x_j)^n \tag{14}$$

where ${}^0 C_{lm}^i$ is the elastic constant of species I, and ${}^n I_{lm}^{ij}$ is the n-order binary interaction parameter between species i and j.

2.4 Experimental methods

High-purity ultrafine powders of TiB_2, NbB_2, and TaB_2 were mixed by a planetary ball mill and then sintered by hot pressing at 2000 °C and pressurized at 30 MPa to prepare diboride. An X-ray diffractometer (XRD; MiniFlex 600, Rigaku, Japan) with Cu Kα radiation from 20° to 90° with a step size of 0.01 at a scanning rate of 2 (°)/min was used to determine the physical phase structure of the diborides ceramic bulks. A scanning electron microscope (SEM; SIGMA-300, ZEISS, Germany) was employed to observe the microscopic morphology, and an energy dispersive spectroscope (EDS; EVO 180, Zeiss, Germany) equipped with SEM was used for local surface scanning to obtain the elemental distribution. Nanomechanical properties can be obtained by using the continuous stiffness model of the nanoindentation single point test. This model can obtain the changes in indentation depth, hardness, and modulus of the sample with the load, the load used is 50 mN, and the load holding time is 30 s.

3 Results and discussion

3.1 Stability screening

Before screening alloy elements for K_{IC} enhancement, it is crucial to ensure that these elements can stably dissolve in TiB_2 without precipitating or decomposing. Thus, both thermodynamic and dynamic stability are discussed in Fig. 2. The ΔH_{mix} of $(TiM)B_2$, after dissolving 29 different elements, is plotted in Fig. 2(a). Negative ΔH_{mix} values typically indicate an element's ability to dissolve in the TiB_2 lattice. Fig. 2(a) shows that the dissolution of Nb, Ta, Mo, W, Tc, Re, and Os in TiB_2 maintains a negative ΔH_{mix}, suggesting stable dissolution in TiB_2. Given that TiB_2 often operates at temperatures above room temperature, even exceeding 1500 K, we consider elements with ΔH_{mix} less than 0.03 eV/atom as candidates. This takes into account the increase in entropy's contribution to Gibbs free energy at higher temperatures. As the temperature rises, entropy can lead to a negative mixing Gibbs free energy even for structures with positive ΔH_{mix}, indicating potential solid solubility. Based on this criterion, 16 elements (Al, Sc, V, Cr, Nb, Mn, Zr, Ta, Ru, Hf, Mo, W, Tc, Re, Os, and Ir) are identified as potential alloying elements for TiB_2. It is important to note that ΔH_{mix} calculations are based on the dilute model, which helps initially screen elements that can dissolve in solution. The impact of compositional changes will be discussed later.

The phonon spectrum and formation enthalpy of MB_2, shown in Figs. 2(b) and 2(c), verify the dynamic and thermodynamic stability. Notably, MB_2's stability in both aspects prevents phase transitions or decomposition of $(TiM)B_2$. Acoustic phonon softening typically signals structural transformation and dynamic instability. In Fig. 2(b), the phonon spectra of AlB_2, ScB_2, VB_2, ZrB_2, NbB_2, MoB_2, TcB_2, HfB_2, and TaB_2 show no imaginary frequencies, indicating dynamic stability. In convex hull graphs, energy above the hull greater than zero indicates thermodynamic instability. Although stable HCP structures for LaB_2, TcB_2, CdB_2, and CoB_2 are not found in the Materials Project, the calculated

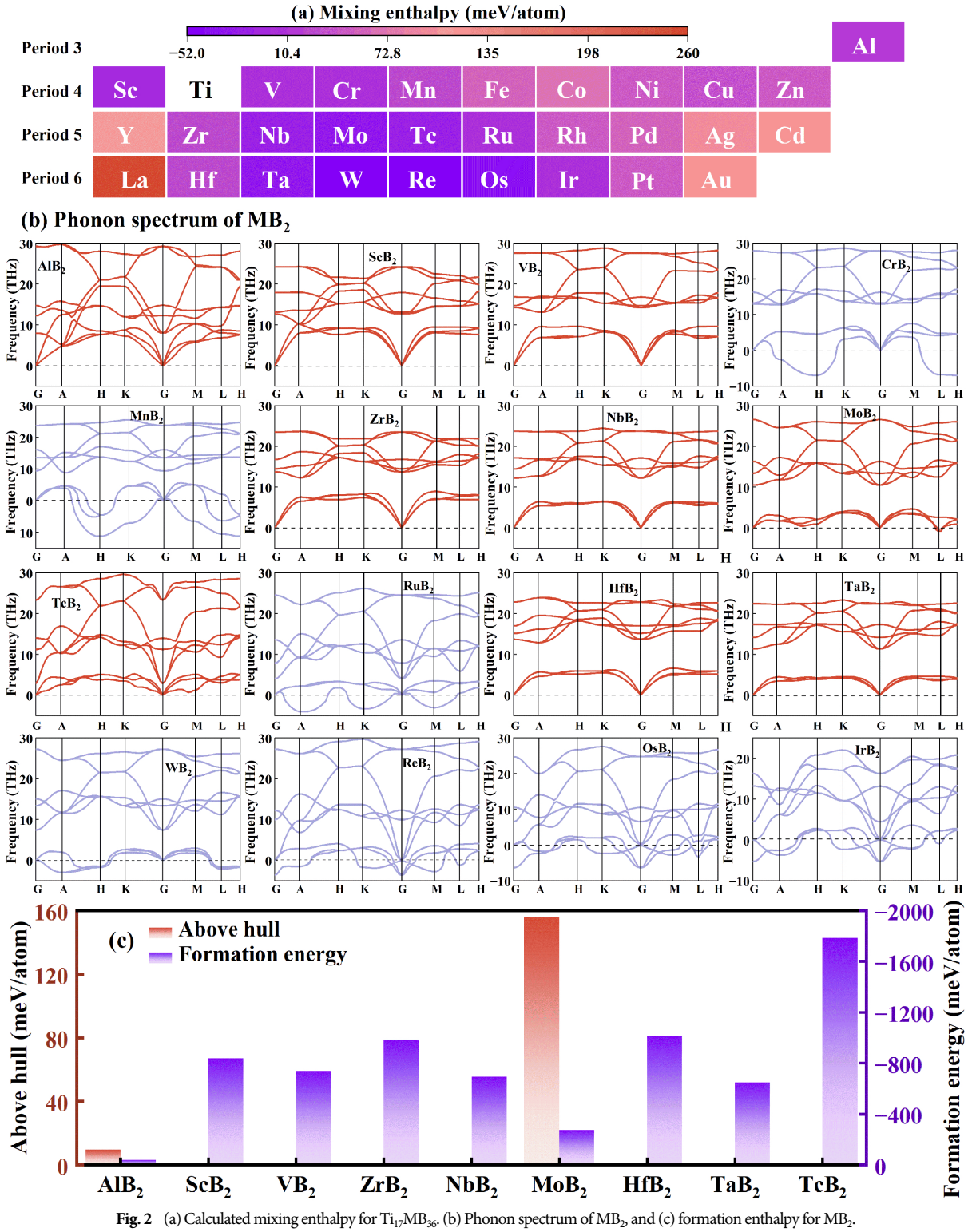

Fig. 2 (a) Calculated mixing enthalpy for $Ti_{17}MB_{36}$. (b) Phonon spectrum of MB_2, and (c) formation enthalpy for MB_2.

formation enthalpy shows that three of them (TcB_2, CoB_2, and LaB_2) have negative formation enthalpies. According to Fig. S4 in the ESM, they lie on the dotted line of the energy convex hull diagram, indicating that these HCP structures are stable.

Based on these standards, thermodynamically stable diborides (ScB_2, VB_2, ZrB_2, NbB_2, TcB_2, HfB_2, and TaB_2) are identified in Fig. 2(c) with zero energy above the hull. It should be noted that these elements are proposed based on their solubility in TiB_2. For other elements' stability, we have also calculated phonons and formation enthalpy. The results are provided in Fig. S5 and Table S1 in the ESM, as they do not meet our criteria and will not be further discussed here.

3.2 Mechanical property screening

To identify alloying elements that improve TiB_2 toughening efficacy while minimizing H_v degradation, mechanical characterization is initiated using a dilute solid-solution model. This approach systematically isolated the individual solute atom effects by employing a single-atom approximation, thereby eliminating intersolute interaction complexities during

preliminary property evaluation. The accuracy of our computational parameter settings is validated through a comparison of C_{ij}, as illustrated in Fig. S6 in the ESM, and the calculated values are in good agreement with the experimental values [42,43]. Figure S6 in the ESM systematically plots the valence electron concentration (VEC)-dependent evolution of *B*, *G*, *E*, H_v, *v*, and *B*/*G*. *B* maintains remarkable stability under Zr, Rh, Hf, and Ir doping, as evidenced in Fig. S7(a) in the ESM. Transition metal dopants (Cr, Mn, Nb, Mo, Tc, Ru, Ta, W, Re, and Os) conversely induce progressive *B* enhancement following VEC increase, with maximum enhancement observed in the Redoped configurations. The doping of other elements results in a decrease in *B*. Other alloying elements result in a decrease in *B*. It is well established that *B* measures a material's ability to resist volume changes; thus, a higher concentration of valence electrons in more electronegative elements makes the valence electron cloud less mobile under external forces, resulting in a larger *B*. Figures S7(b) and S5(c) in the ESM demonstrate a clear trend in *E* that mirrors that of *G*. Specifically, as the concentration of valence electrons increases, *E* initially decreases before ascending, reaching a minimum value at a VEC of approximately 10.3 to 10.4 e/a. Notably, the *E* of the $Ti_{17}WB_{36}$ dilute solid solution exhibits the highest value. *G* remains relatively stable when M is Sc, Zr, Nb, Mo, Hf, or Ta; however, *G* shows a declining trend with the introduction of other atoms.

Figure 3(a) summarizes the key properties that quantify the influence of alloying elements on H_v, K_{IC}, *E*, and *B*/*G*. The solid solution maintains a lower H_v than pure TiB_2, and the elements that weaken the H_v by 10% are V, Ti, Cr, Mo, Zr, Nb, Mn, Hf, Ta, and W. The calculated K_{IC} and *B*/*G* values indicate that elements including Au, Pt, Ir, Os, Re, W, Ta, Hf, Rh, Ru, Tc, Mo, Nb, Ni, Mn, and Cr can enhance the K_{IC} and plasticity of TiB_2. After a comprehensive evaluation of the balance between H_v and K_{IC}, Zr, Sc, V, Nb, Mo, Tc, Ta, Hf, and Al are selected as alloying elements for further investigation into their effects on mechanical properties. After the screening of the kinds of elements, composition-dependent mechanical properties are obtained by the CALPHAD fitting approach, as illustrated in Fig. 3(b). Initially, the ΔH_{mix} is negative across the range of alloy compositions. Regarding the composition dependence of H_v, eight elements, except Zr, show a decreasing trend in H_v with increasing alloy composition, with solid solutions of Sc, Hf, and V demonstrating lower sensitivity to compositional changes. *B*/*G* showed a reverse trend, increasing with increasing concentration. For K_{IC}, the trend is not always strictly monotonic with increasing concentrations of alloying elements. This result indicated that Mo, Nb, Hf, Ta, and Zr with a concentration of 50 at% are the best solid solution candidates for TiB_2. The elastic properties of the CALPHAD fit are verified by DFT calculations, as shown in Fig. S8 in the ESM, and the difference between them is less than 3%, which proves that the CALPHAD method has excellent fitting ability for the mechanical properties of diboride.

3.3 Toughness enhancement via configurational entropy

Building on this framework, toughening elements for titanium diboride were first screened using a dilute solid-solution model, while the optimal compositional ranges were identified through CALPHAD calculations. Multicomponent diborides with varying numbers of constituents were then constructed, enabling a systematic evaluation of the toughness evolution with increasing configurational entropy via calculated fracture toughness. To elucidate the influence of configurational entropy (S_{config}) on the toughness of HEBs, we systematically evaluated four classical mechanical parameters that serve as proxies for material toughness, as shown in Fig. 4, the formula of S_{config} as Eq. (15):

$$S_{config} = -R\sum_{i=1}^{m} x_i \ln x_i \tag{15}$$

where *R* is the ideal gas constant, and x_i is the molar fraction of

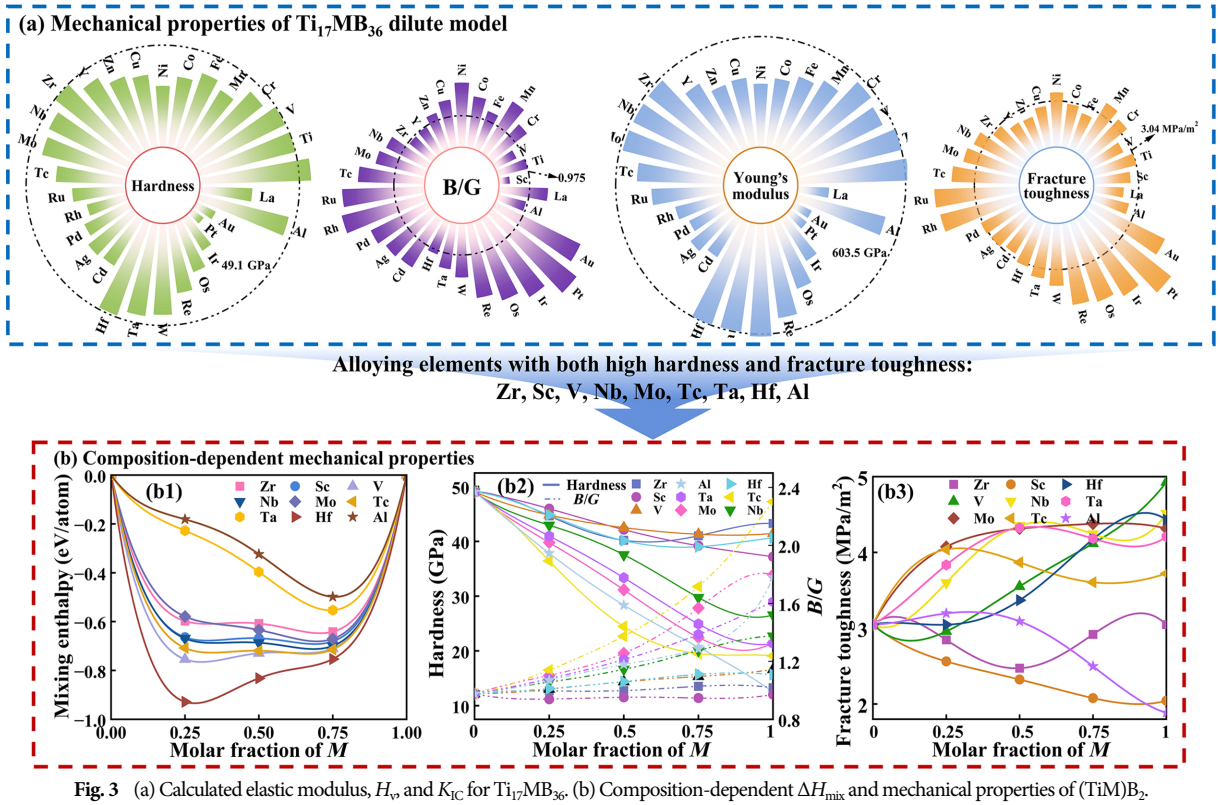

Fig. 3 (a) Calculated elastic modulus, H_v, and K_{IC} for $Ti_{17}MB_{36}$. (b) Composition-dependent ΔH_{mix} and mechanical properties of $(TiM)B_2$.

dibories *i*. These include (i) fracture toughness (K_{IC}), which directly reflects resistance to crack propagation; (ii) Poisson's ratio (ν), indicative of the material's ability to nucleate dislocations and accommodate stress near crack tips; (iii) the B/G ratio, representing the barrier to dislocation slip; and (iv) the elastic modulus descriptor $(C_{12}-C_{44})/E$, which reflects bonding character—where more negative values imply stronger covalent bonding.

As the trends demonstrate in Figs. 4(a)–4(d), for 4HEB (S_{config} = 11.53 J/(mol·K)) and 5HEB (S_{config} = 13.38 J/(mol·K)), compositions containing vanadium (e.g., 4HEB-1, 5HEB-1, 5HEB-3) exhibit significantly reduced toughness relative to those without vanadium. However, the introduction of high configurational entropy plays a compensating and even overriding role: As the number of principal components increases from quaternary to secondary systems, the overall toughness is enhanced. This remains true even when certain elemental combinations cause local decreases in toughness, highlighting the dominant and beneficial role of entropy. In 6HEB compositions, the calculated K_{IC} is close to 6 MPa·m$^{1/2}$, ν is over 0.24, and $(C_{12}-C_{44})/E$ is close to 0, suggesting a potential ductile ceramic. Notably, the predicted fracture toughness and hardness values for the 5HEB-2 composition are in strong agreement with experimental results [44,45], with a discrepancy of less than 10%. This validates the computational methods employed in this study and underscores their reliability for mechanical property prediction in multicomponent borides.

The relationship between K_{IC} and S_{config} is initially established through high-precision first-principles calculations, revealing that increasing S_{config} significantly enhances the toughness of HEBs. However, the underlying physical mechanism remains to be fully elucidated. To this end, we explore two critical descriptors of bonding physics: δ and the COHP. While δ has frequently been discussed in previous studiesparticularly in relation to hardness, its connection to toughness remains less defined. COHP, on the other hand, offers direct insight into bond strength evolution and provides a robust framework for understanding the fundamental nature of entropy-induced toughening. Figure 5(a) quantifies δ across binary to senary diboride systems, calculated as the root-mean-square deviation between relaxed and ideal atomic positions. Figures 5(b) and 5(c) present the integrated COHP (–ICOHP) and the projected COHP (–pCOHP), respectively, capturing the evolution of bonding interactions as a function of increasing entropy.

Overall, δ exhibits a positive correlation with toughness: As S_{config} increases, structural lattice distortion becomes more pronounced, aligning with improved toughness. However, deviations from this trend highlight its nonessential role. For instance, 4HEB-1 exhibits greater δ than 4HEB-2 but demonstrates lower toughness. Similarly, 5HEB-3 shows only a marginal increase in δ over 4HEB-3 but displays a significantly enhanced toughness. These inconsistencies suggest that while δ contributes to the overall behavior, it is not the primary driver of toughness enhancement. More decisive insights are revealed by the COHP analysis. As shown in Fig. 5(b), –ICOHP values for M–B bonds in binary and ternary diborides exhibit wide variations. For example, Nb–B bonds show very low bonding strength (~0.1), whereas Ta–B bonds reach up to ~2.4. For 4HEB-2 and 5HEB-2, the average ICOHP values are 1.726 and 1.722, respectively; nevertheless, the corresponding K_{IC} values increase by more than 1 MPa·m$^{1/2}$, indicating that enhanced S_{config} effectively

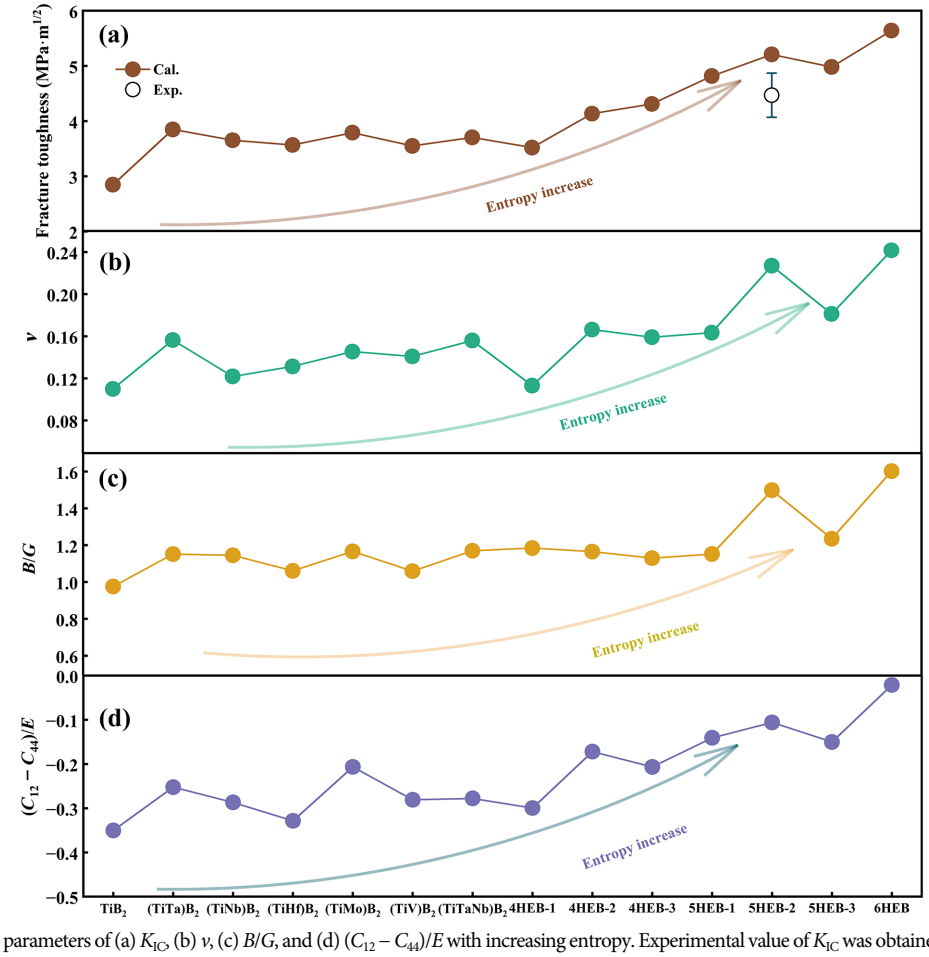

Fig. 4 Critical parameters of (a) K_{IC}, (b) ν, (c) B/G, and (d) $(C_{12}-C_{44})/E$ with increasing entropy. Experimental value of K_{IC} was obtained from Ref. [45].

promotes the toughness of MB_2. With increasing S_{config}, M–B bond strengths converge toward an averaged value, particularly through the strengthening of previously weak bonds (e.g., Nb–B, V–B). By the time a six-component composition is reached, these bonds exhibit comparable strength across species, resulting in a homogenized bonding environment. This phenomenon—entropy-induced bond averaging correlates closely with observed increases in fracture toughness. Specifically, weak M–B bonds (e.g., V–B) present in lower-entropy systems contribute to early crack nucleation under stress. As entropy increases, the density of such weak bonds decreases, leading to a higher average bond strength and improved resistance to fracture. Further evidence is provided in Fig. 5(c), which displays the –pCOHP spectra for first-nearest-neighbor M–B and Ti–B bonds. The –pCOHP values delineate bonding (negative), nonbonding (zero), and antibonding (positive) interactions. Below the Fermi level (E_f), both M–B and Ti–B bonds exhibit clear bonding character. Notably, with increasing entropy, the bonding peaks of different metal–boron interactions converge in magnitude, underscoring the uniformization of bond strength. The entropy-induced broadening of the bond-strength trap reduces the anisotropy and directionality of individual M–B bonds. This bond delocalization alleviates stress concentration at crack tips, thereby promoting more homogeneous deformation and enhancing the overall fracture toughness. Furthermore, supplementary analysis of the B–B bonds (Fig. S9 in the ESM) reveals that their strength also decreases with increasing configurational entropy, which further contributes to toughening by mitigating the brittleness associated with strong, planar covalent B–B networks.

3.4 DFT-assisted experimental verification

Based on the screening results, the compounds $(TiTa)B_2$, $(TiNb)B_2$, and $(TiNbTa)B_2$ are synthesized using hot-pressing sintering. Their phase structures and physical properties are characterized, as shown in Fig. 6. The X-ray diffraction patterns of the synthesized materials—TiB_2, $(TiTa)B_2$, $(TiNb)B_2$, and $(TiNbTa)B_2$ are illustrated in Fig. 6(a). All diborides exhibit characteristic peaks consistent with TiB_2, with peak positions aligning with the standard PDF card. The incorporation of Ta and Nb results in a leftward shift of these characteristic peaks, confirming that the three borides are single-phase solid solutions. Figure 6(b) presents the SEM-EDS analysis results for TiB_2, $(TiTa)B_2$, $(TiNb)B_2$, and $(TiNbTa)B_2$. The SEM images reveal no significant secondary phases in the four-component diborides, while EDS characterization indicates a uniform distribution of elements across the scanned surfaces. This confirms the successful synthesis of single-phase multicomponent diborides, validating our stability calculations. These results suggest that the alloy components identified through our screening criteria can form stable single-phase solid solutions. To assess the mechanical properties of the synthesized samples, we performed nanoindentation tests. The H_v and E values are presented in Fig. 6(c). Due to the brittle nature of diborides, evaluating K_{IC} using single-sided notched beam methods is challenging, as specimen processing is intricate and results can be unreliable. Instead, we qualitatively assessed K_{IC} by analyzing the displacement differences observed during nanoindentation at the same load; larger displacement values indicate improved K_{IC}.

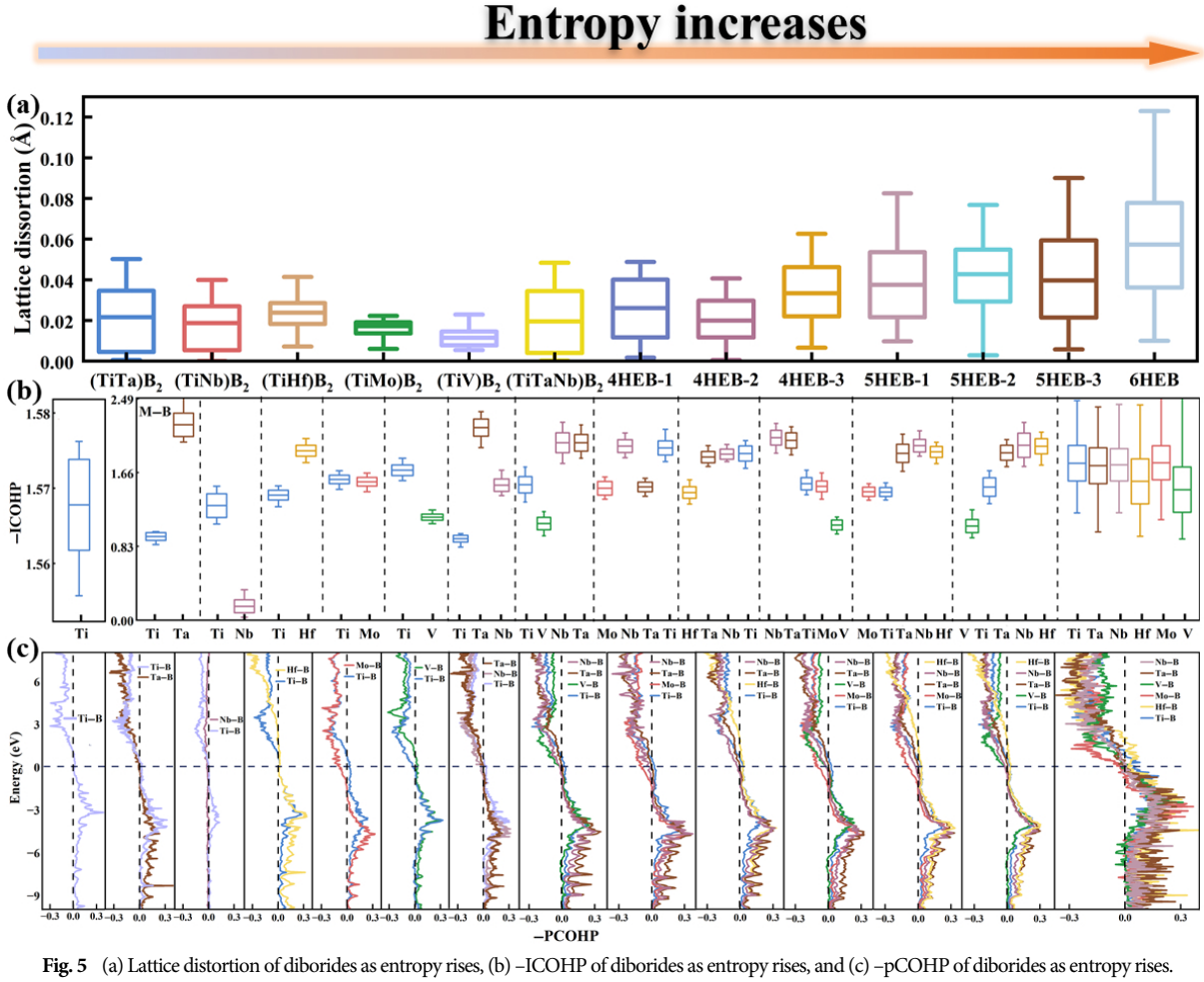

Fig. 5 (a) Lattice distortion of diborides as entropy rises, (b) –ICOHP of diborides as entropy rises, and (c) –pCOHP of diborides as entropy rises.

清華大学出版社 Tsinghua University Press | SciOpen

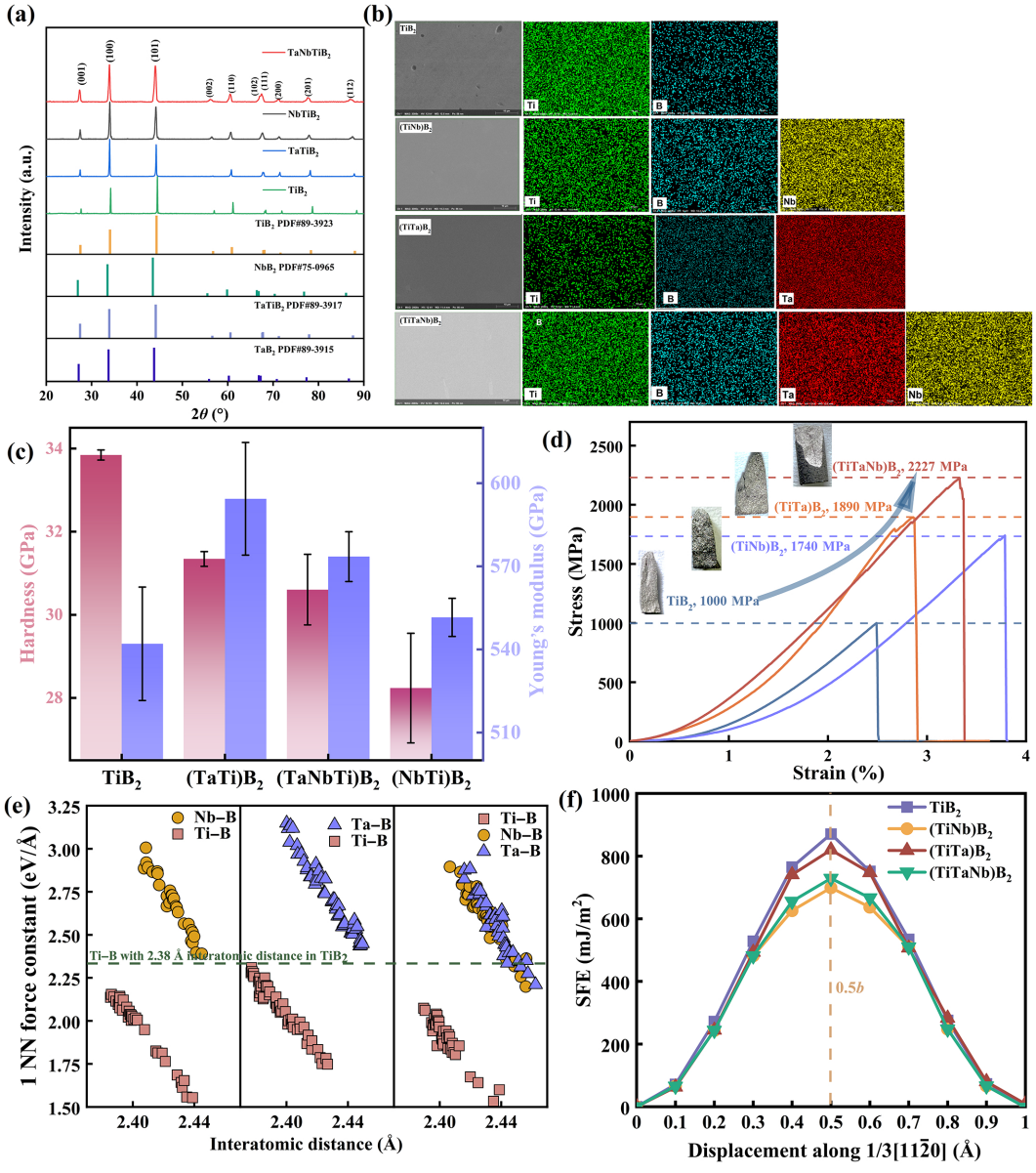

Fig. 6 (a) X-ray diffraction patterns of TiB_2, $(TiTa)B_2$, $(TiNb)B_2$, and $(TiNbTa)B_2$. (b) SEM-EDS analysis results of TiB_2, $(TiTa)B_2$, $(TiNb)B_2$, and $(TiNbTa)B_2$. (c) H_v and E obtained by nanoindentation. (d) Compressive stress-strain curves, (e) calculated 1NN force constants, and (f) calculated GSFE.

According to the data in Fig. 6(d), the solid solution containing Nb exhibits the best extensibility, although this improvement is accompanied by a more significant reduction in H_v. In contrast, the Ta-doped sample shows the lowest extensibility. Second, the test results of compressive strength show that ternary diboride has the highest compressive strength, with a value of 2227 MPa, followed by $(TaTi)B_2$ with a compressive strength of 1890 MPa, $(TiNb)B_2$ with a compressive strength of 1740 MPa, and pure TiB_2 with a value of 1000 MPa. For the change in strength and plasticity of diboride, we further calculated the phonon force constant and stacking fault energy to provide more evidence of the influence of elements. The calculated 1NN stretch force constants (SFCs) and interatomic distances between the Ti, Ta, Nb, and B atoms in the first coordination shell are depicted in Fig. 6(e). The phonon spectrum is plotted in Fig. S8 in the ESM. For the compounds $(TiTa)B_2$ and $(TiNb)B_2$, the SFCs for Ta–B and Nb–B (2.4–3.2 and 2.39–3.0 eV/Å, respectively) are higher than the Ti–B SFC (2.38 eV/Å) in pure TiB_2. However, the Ti–B bond strength is diminished in $(TiTa)B_2$ and $(TiNb)B_2$ due to lattice distortion, which results in lower SFCs and increased interatomic distances. This reduction explains why the H_v of TiB_2 is greater, while its K_{IC} is lower compared to $(TiTa)B_2$ and $(TiNb)B_2$. In the case of $(TiNbTa)B_2$, although the Ti–B bond exhibits the lowest SFCs, the number of Ti–B bonds is fewer than in the other diborides. From a phonon perspective, the enhancement of K_{IC} in titanium diboride due to alloying elements arises from the introduction of M–B bonds with high SFCs while simultaneously weakening the Ti–B bond. As shown in Fig. 6(f), the generalized stacking fault energy (GSFE) validates that the stacking fault energy is lower following the incorporation of

Table 1 Microhardness and elastic modulus of TiB_2, $(TiTa)B_2$, $(TiNb)B_2$, and $(TiNbTa)B_2$

Space	H_v (GPa)	E (GPa)
TiB_2	33.1±3.5	539.9±12.2
$(TiTa)B_2$	30.5±2.6	559.7±15.6
$(TiNb)B_2$	28.5±2.1	594.4±16.3
$(TiNbTa)B_2$	31.2±1.9	572.3±17.2

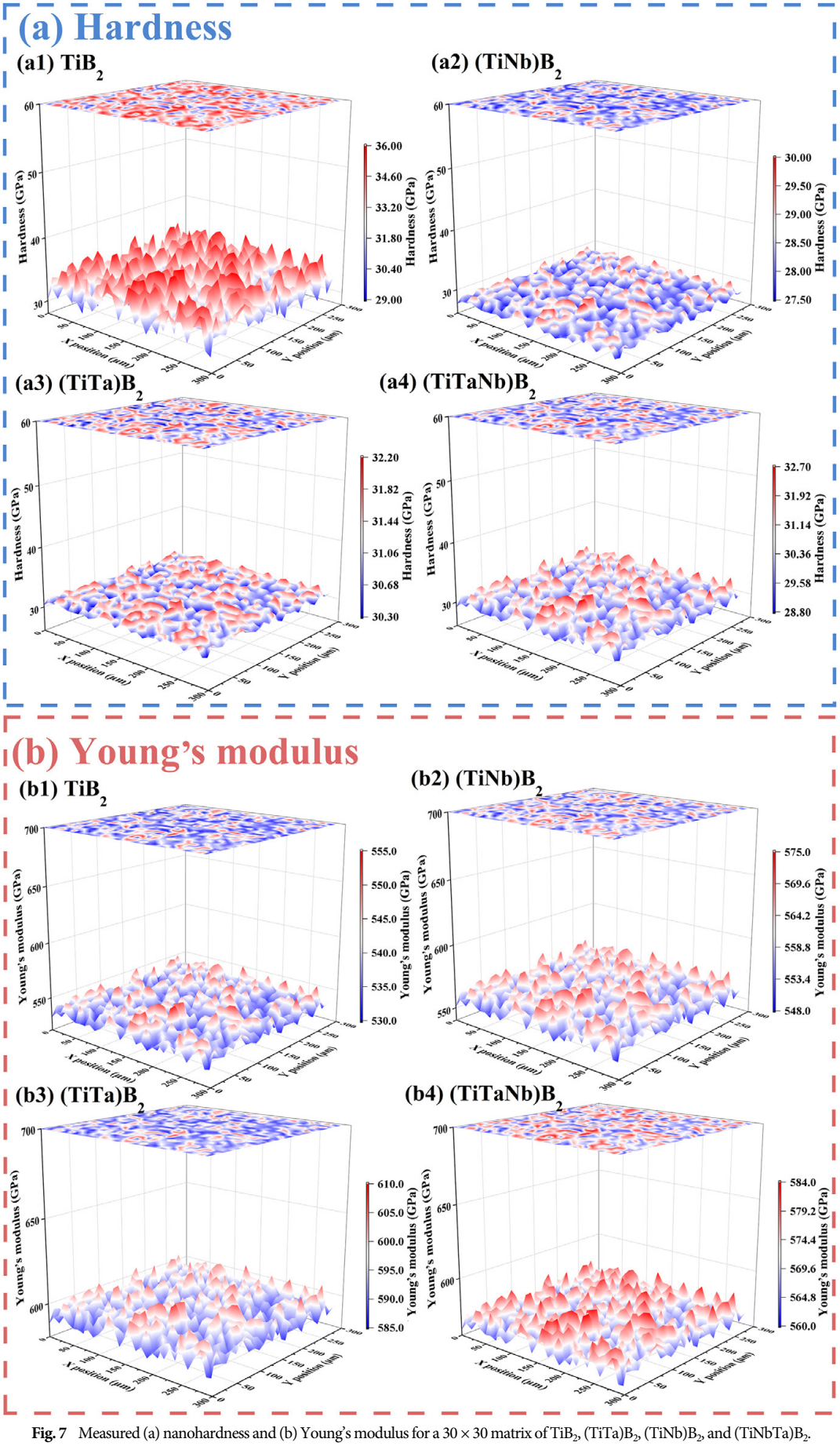

Fig. 7 Measured (a) nanohardness and (b) Young's modulus for a 30 × 30 matrix of TiB_2, $(TiTa)B_2$, $(TiNb)B_2$, and $(TiNbTa)B_2$.

https://doi.org/10.26599/JAC.2026.9221266

$(TiNb)B_2$ compared to $(TiTa)B_2$. The stacking fault energy determines the potential barrier of slip. In origin, the reduction in stacking fault energy comes from the reduction in the M–B bond. The difference is that the strong Ta–B bond weakens the bond strength of Ti–B in the Ti–Ta–B system, while the weak Nb–B bond is introduced in the Ti–Nb–B system.

To minimize errors in mechanical property evaluation caused by microstructural heterogeneity and the limitations of the random single-indentation approach (i.e., the continuous stiffness method), the mechanical properties of each sample are systematically characterized using the 3D nanoBlitz technique under a constant load of 50 mN. The resulting data are presented as two-dimensional maps of microhardness and elastic modulus in Fig. 7 and Table 1. This high-throughput approach enables robust statistical analysis of spatial property distributions. The indentation results reveal that hardness values exhibit limited variation across the sampled area, indicating a high degree of compositional uniformity in the sintered boride and the absence of significant elemental segregation or secondary phase precipitation. The observed fluctuations in mechanical properties are primarily attributed to microstructural defects introduced during the sintering process, which can result in incomplete densification of the bulk material.

Furthermore, to assess the performance of diboride ceramics under realistic service conditions, their thermodynamic and mechanical properties at elevated temperatures were systematically evaluated. The Gibbs free energy considering the vibration can be written as Eq. (16) [46]:

$$\Delta G(x, T, P) = \Delta H - T\Delta S + \Delta A \tag{16}$$

where, ΔH is the mixing enthalpy, ΔS is the configuration entropy, and ΔA is the mixing vibrational free energy, which is given by Eqs. (17) and (18):

$$\Delta A = \mathrm{M}\sum\nolimits_{j=1}^{J} p_j \varepsilon_j \tag{17}$$

$$\varepsilon_j = A - \frac{n - n_j}{n} A_1 - \frac{n_j}{n} A_2 \tag{18}$$

A_i is the total energy of single diborides i and M is the total number of alloying elements. F_{vib} represents the contribution of lattice vibrations to the free energy, which can be calculated from the phonon density of states at the corresponding volume (Eq. (19)) [47]:

$$F_{vib}(V, T) = k_B T \int_0^{\infty} \ln\left(2\sinh\frac{\hbar\omega}{2k_B T}\right) g(\omega)\,\mathrm{d}(\omega) \tag{19}$$

Here, the ω represents the phonon frequency, T represent the temperature. The linear thermal expansion coefficient $\alpha(T)$ is calculated by Eq. (20):

$$\alpha(T) = \frac{1}{3V_{eq}(T)}\left(\frac{\partial V_{eq}(T)}{\partial T}\right)_P \tag{20}$$

where V_{eq} represent the volume at equal state. The procedure for calculating the temperature-dependent isothermal elastic constants ($C_{ij}(T)$) can be summarized in three steps as follows: (i) calculating the static elastic constants at 0 K as a function of volume $C_{ij}(V)$ using the stress-strain energy method; (ii) predicting the volume change as a function of temperature at ambient pressure $V(T, 0)$ using the quasiharmonic approximation; (iii) deriving the temperature dependence of isothermal elastic constants as $C_{ij}(T) = C_{ij}(T(V))$ [47].

Using the aforementioned thermodynamic and mechanical frameworks, the temperature-dependent properties of representative diborides were evaluated, as summarized in Fig. 8. In Fig. 8(a), the parameters of the Debye model were calibrated against experimental thermal expansion coefficients, enabling evaluation of the Gibbs free energy of mixing. Temperature-dependent mechanical properties were subsequently derived from the thermally induced volume expansion within the quasistatic approximation, as shown in Figs. 8(b)–8(f). The results indicate that increasing configurational entropy further lowers the Gibbs free energy across the investigated temperature range, thereby enhancing high-temperature structural stability. The deviation between the calculated and experimental mechanical properties remains within 15%, supporting the reliability of the computational approach. These temperature-resolved mechanical

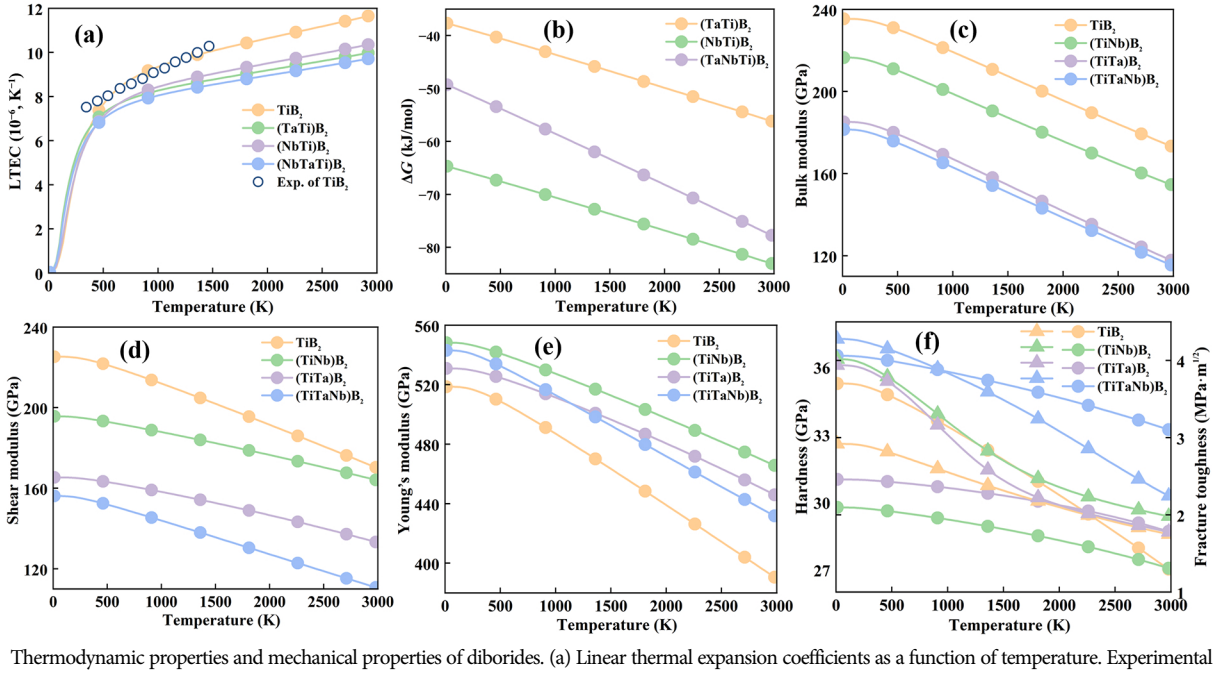

Fig. 8 Thermodynamic properties and mechanical properties of diborides. (a) Linear thermal expansion coefficients as a function of temperature. Experimental values were obtained from Ref. [48]. (b) Gibbs mixing free energy, (c) bulk modulus, (d) shear modulus, (e) Young's modulus, and (f) hardness and fracture toughness.

data provide a quantitative basis for assessing the high-temperature applicability of diboride ceramics.

4 Conclusions

In this work, based on the systematic screening of alloying elements and their effects on mechanical properties, binary and multicomponent diborides are chosen to clarify the influence of the changes in alloying elements and configuration entropy on the H_v, K_{IC}, strength, and plasticity of titanium diboride. Through the calculation of lattice distortion, electronic structure, phonon and stacking fault energy, the main conclusions are as follows:

(1) Starting from single-component TiB_2, a process-oriented strategy for screening toughening elements is established. Elemental species are first identified using a dilute solid-solution model that suppresses periodic image interactions, while the TiB_2 fraction in the matrix is progressively increased. Composition-dependent properties, including hardness and fracture toughness, are then derived through CALPHAD-based fitting, leading to the identification of Ta, Nb, Mo, Hf, and V as candidate elements with equiatomic compositions.

(2) Based on the screening results, multicomponent diborides containing two to six elements are constructed, and entropy-dependent toughness is evaluated using B/G, K_{IC}, and related metrics. The calculations are validated against available experimental data, revealing a clear toughness enhancement with increasing configurational entropy. Subsequent COHP analysis indicates that the elevated K_{IC} arises from an entropy-driven expansion of the bond-strength trap, which diminishes the anisotropy and directionality of individual M–B bonds.

(3) Single-phase $(TiTa)B_2$, $(TiNb)B_2$, and $(TiNbTa)B_2$, which preserve maximal M–B bond-strength contrast, are successfully synthesized, with H_v and K_{IC} experimentally confirmed. Nb and Ta incorporation facilitates dislocation slip and enhances plasticity, while force-constant analysis correlates the improved compressive strength with strengthened interatomic bonding.

Acknowledgements

The authors would like to thank the financial support from the Yunnan Fundamental Research Projects (No. 202501AS070137), the Yunnan Major Scientific and Technological Projects (No. 202302AG050010) and the open research fund of the National Key Laboratory of Marine Corrosion and Protection and the Major R&D Project of Yunnan Province (No. 202402AB080007).

Author contributions

The manuscript is written through the contributions of all authors. All authors have approved the final version of this manuscript.

Availability of data and materials

The data that support the findings of this study are available from the corresponding author upon reasonable request.

Competing interest

The authors have no competing interests to declare that are relevant to the content of this article. The author Jing Feng is the Editorial Committee member of this journal

Electronic Supplementary Material

Supplementary material is available in the online version of this article at https://doi.org/10.26599/JAC.2026.9221266.

References

[1] Chen XQ, Fu CL, Krčmar M, *et al.* Electronic and structural origin of ultraincompressibility of 5d transition-metal diborides MB_2 (M = W, Re, Os). *Phys Rev Lett* 2008, **100**: 196403.

[2] Wicher B, Pshyk OV, Li X, *et al.* Superhard oxidation-resistant $Ti_{1-x}Al_xB_y$ thin films grown by hybrid HiPIMS/DCMS co-sputtering diboride targets without external substrate heating. *Mater Des* 2024, **238**: 112727.

[3] Chung HY, Weinberger MB, Levine JB, *et al.* Synthesis of ultra-incompressible superhard rhenium diboride at ambient pressure. *Science* 2007, **316**: 436–439.

[4] Monteverde F. The thermal stability in air of hot-pressed diboride matrix composites for uses at ultra-high temperatures. *Corros Sci* 2005, **47**: 2020–2033.

[5] Feng L, Fahrenholtz WG, Hilmas GE, *et al.* Strength retention of single-phase high-entropy diboride ceramics up to 2000 °C. *J Am Ceram Soc* 2024, **107**: 1895–1904.

[6] Kang SH, Kim DJ. Synthesis of nano-titanium diboride powders by carbothermal reduction. *J Eur Ceram Soc* 2007, **27**: 715–718.

[7] Xie T, Li WD, Velisa G, *et al.* An overview of high-throughput synthesis for advanced high-entropy alloys. *Mater Genome Eng Adv* 2025, **3**: 87.

[8] Jin XZ, Luo H, Wang XF, *et al.* Data mining accelerated the design strategy of high-entropy alloys with the largest hardness based on genetic algorithm optimization. *Mater Genome Eng Adv* 2024, **2**: 49.

[9] Oses C, Toher C, Curtarolo S. High-entropy ceramics. *Nat Rev Mater* 2020, **5**: 295–309.

[10] Xu YX, Yu L, Zhao T, *et al.* Composition design of oxidation resistant non-equimolar high-entropy ceramic materials: An example of $(Zr–Hf–Ta–Ti)B_2$ ultra-high temperature ceramics. *J Adv Ceram* 2024, **13**: 2087–2100.

[11] Liu Y, Lu YH, Wang WY, *et al.* Effects of solutes on thermodynamic properties of (TMZrU)C (TM = Ta, Y) medium-entropy carbides: A first-principles study. *J Mater Inf* 2023, **3**: 17.

[12] Mhadeshwar A, Mohanty T, Sparks TD. Borides as promising M_2AX phase materials with high elastic modulus using machine learning and optimization. *J Mater Inf* 2024, **4**: 12.

[13] Li J, He L, Peng F, *et al.* Optimized process and superior toughness of a (HfNbTaTiW)C high entropy carbide ceramic. *Ceram Int* 2024, **50**: 32129–32137.

[14] Tang ZY, Wen ZH, Liu YW, *et al.* Rapid experimental screening of high-entropy diborides for superior oxidation resistance. *Adv Funct Mater* 2024, **34**: 2312239.

[15] Liu YW, Ma MD, Wang W, *et al.* Lattice distortion enhanced hardness in high-entropy borides. *Adv Funct Mater* 2025, **35**: 2416992.

[16] Qin MD, Gild J, Wang HR, *et al.* Dissolving and stabilizing soft WB_2 and MoB_2 phases into high-entropy borides via boron-metals reactive sintering to attain higher hardness. *J Eur Ceram Soc* 2020, **40**: 4348–4353.

[17] Liu JX, Shen XQ, Wu Y, *et al.* Mechanical properties of hot-pressed high-entropy diboride-based ceramics. *J Adv Ceram* 2020, **9**: 503–510.

[18] Basu B, Raju GB, Suri AK. Processing and properties of monolithic TiB_2 based materials. *Int Mater Rev* 2006, **51**: 352–374.

[19] Kempa KA, Karch J, Wrona IA, *et al.* Electronic and optical properties of monolayer magnesium diboride under biaxial strain. *Comput Mater Sci* 2025, **246**: 113343.

[20] Aydın H, Kurtan Ü, Üstün B, *et al.* A preparation of niobium diboride (NbB_2) via molten salt method: Impact of boron concentration on the structural and electrochemical performance. *Mater Res Bull* 2024, **180**: 113062.

[21] Rout CS, Shinde PV, Patra A, *et al.* Recent developments and future perspectives of molybdenum borides and MBenes. *Adv Sci* 2024, **11**: 2308178.

[22] van de Walle A, Tiwary P, de Jong M, *et al.* Efficient stochastic

generation of special quasirandom structures. *Calphad* 2013, **42**: 13–18.
[23] Kresse G, Hafner J. *Ab initio* molecular-dynamics simulation of the liquid–metal–amorphous-semiconductor transition in germanium. *Phys Rev B* 1994, **49**: 14251–14269.
[24] Kresse G, Furthmüller J. Efficiency of *ab-initio* total energy calculations for metals and semiconductors using a plane-wave basis set. *Comp Mater Sci* 1996, **6**: 15–50.
[25] Kresse G, Hafner J. *Ab initio* molecular dynamics for liquid metals. *Phys Rev B* 1993, **47**: 558–561.
[26] Kresse G, Hafner J. Norm-conserving and ultrasoft pseudopotentials for first-row and transition elements. *J Phys: Condens Matter* 1994, **6**: 8245–8257.
[27] Ernzerhof M, Scuseria GE. Assessment of the Perdew–Burke–Ernzerhof exchange-correlation functional. *J Chem Phys* 1999, **110**: 5029–5036.
[28] Gan MD, Lu TL, Yu W, *et al.* Capturing and visualizing the phase transition mediated thermal stress of thermal barrier coating materials via a cross-scale integrated computational approach. *J Adv Ceram* 2024, **13**: 413–428.
[29] Monkhorst HJ, Pack JD. Special points for Brillouin-zone integrations. *Phys Rev B* 1976, **13**: 5188–5192.
[30] Chong XY, Yu W, Liang YX, *et al.* Understanding oxidation resistance of Pt-based alloys through computations of Ellingham diagrams with experimental verifications. *J Mater Inf* 2023, **3**: 21.
[31] Dai FZ, Wen B, Sun YJ, *et al.* Theoretical prediction on thermal and mechanical properties of high entropy $(Zr_{0.2}Hf_{0.2}Ti_{0.2}Nb_{0.2}Ta_{0.2})C$ by deep learning potential. *J Mater Sci Technol* 2020, **43**: 168–174.
[32] Shang S, Böttger AJ. A combined cluster variation method and *ab initio* approach to the γ-Fe [N]/γ′-Fe_4N_{1-x} phase equilibrium. *Acta Mater* 2005, **53**: 255–264.
[33] Hillert M, Staffansson LI. The regular solution model for stoichiometric phases and ionic melts. *Acta Chem Scand* 1970, **24**: 3618–3626.
[34] Ouerfelli N, Iulian O, Bouaziz M. Competition between Redlich–Kister and improved Herráez equations of correlation viscosities in 1,4-dioxane + water binary mixtures at different temperatures. *Phys Chem Liq* 2010, **48**: 488–513.
[35] Hill R. The elastic behaviour of a crystalline aggregate. *P Phys Soc A* 1952, **65**: 349–354.
[36] Feng XL, Zhang XY, Liu HY, *et al.* Low-density superhard materials: Computational study of Li-inserted B-substituted closo-carboranes $LiBC_{11}$ and $Li_2B_2C_{10}$. *RSC Adv* 2016, **6**: 52695–52699.
[37] Tian YJ, Xu B, Zhao ZS. Microscopic theory of hardness and design of novel superhard crystals. *Int J Refract Met H* 2012, **33**: 93–106.
[38] Chen XQ, Niu HY, Li DZ, *et al.* Modeling hardness of polycrystalline materials and bulk metallic glasses. *Intermetallics* 2011, **19**: 1275–1281.
[39] Liu YH, Chong XY, Jiang YH, *et al.* Mechanical properties and electronic structures of Fe–Al intermetallic. *Physica B* 2017, **506**: 1–11.
[40] Wu ZJ, Zhao EJ, Xiang HP, *et al.* Crystal structures and elastic properties of superhard IrN_2 and IrN_3 from first principles. *Phys Rev B* 2007, **76**: 054115.
[41] Mazhnik E, Oganov AR. A model of hardness and fracture toughness of solids. *J Appl Phys* 2019, **126**: 125109.
[42] Gu XL, Liu C, Guo H, *et al.* Sorting transition-metal diborides: New descriptor for mechanical properties. *Acta Mater* 2021, **207**: 116685.
[43] Zhao JJ, Winey JM, Gupta YM. First-principles calculations of second- and third-order elastic constants for single crystals of arbitrary symmetry. *Phys Rev B* 2007, **75**: 094105.
[44] Zhang Y, Guo WM, Jiang ZB, *et al.* Dense high-entropy boride ceramics with ultra-high hardness. *Scripta Mater* 2019, **164**: 135–139.
[45] Zhang Y, Jiang ZB, Sun SK, *et al.* Microstructure and mechanical properties of high-entropy borides derived from boro/carbothermal reduction. *J Eur Ceram Soc* 2019, **39**: 3920–3924.
[46] Ferreira PN, Lucrezi R, Guilhon I, *et al.* *Ab initio* modeling of superconducting alloys. *Mater Today Phys* 2024, **48**: 101547
[47] Yang Lin, Wei Yu, Guangchi Wang, *et al.* Exploring the effect of alloying elements on the thermoelasticity and strength of bcc Fe-based alloys by first-principles phonon calculations. *J Mater Res Technol* 2024, **30**: 954–965.